Journal of the European Ceramic Society 44 (2024) 7825–7836

Contents lists available at ScienceDirect

Journal of the European Ceramic Society

journal homepage: www.elsevier.com/locate/jeurceramsoc

Fluorite-pyrochlore-weberite phase transitions in a series of 20-component ultrahigh-entropy compositionally complex ceramics

Keqi Song [a], Dawei Zhang [a], Ka Man Chung [a], Renkun Chen [a,b], Jian Luo [a,c,*]

[a] Program in Materials Science and Engineering, University of California San Diego, La Jolla 92093, USA
[b] Department of Mechanical and Aerospace Engineering, University of California San Diego, La Jolla 92093, USA
[c] Aiiso Yufeng Li Family Department of Chemical and Nano Engineering, University of California San Diego, La Jolla, CA 92093, USA

ARTICLE INFO

Keywords:
High-entropy ceramics
Compositionally complex ceramics
Phase transition
Fluorite
Pyrochlore

ABSTRACT

A new series of 20-component fluorite-based compositionally complex oxides (20CCFBO$_{x\mathrm{Nb/Ta}}$) with the general chemical formula $(15RE_{1/15})_{2x+1}(Ce_{1/3}Zr_{1/3}Hf_{1/3})_{3-3x}(Nb_{1/2}Ta_{1/2})_xO_{8-\delta}$ ($0 \le x \le 1$, where $15RE_{1/15} = La_{1/15}Pr_{1/15}Nd_{1/15}Sm_{1/15}Eu_{1/15}Gd_{1/15}Tb_{1/15}Dy_{1/15}Y_{1/15}Ho_{1/15}Er_{1/15}Tm_{1/15}Yb_{1/15}Lu_{1/15}Sc_{1/15}$) are synthesized. Despite that the Gibbs phase rule allows for the existence of up to 20 phases at the thermodynamic equilibrium, 17 of the 20CCFBO$_{x\mathrm{Nb/Ta}}$ compositions synthesized in this study all possess single ultrahigh-entropy phases in fluorite, pyrochlore, or weberite structure, as shown by X-ray diffraction (XRD). Only < 1 vol% of secondary phases are observed in two compositions near the phase-transition points. With changing compositional variable x, this series of 20CCFBO$_{x\mathrm{Nb/Ta}}$ undergoes an abrupt fluorite-pyrochlore transition at $x = \sim 0.27$ and an abrupt pyrochlore-weberite transition at $x = \sim 0.87$. Careful characterization reveals abrupt changes of order parameters at both phase transitions. In addition, weberite short-range ordering can persist into the long-range pyrochlore phase, which leads to the lowest thermal conductivities.

1. Introduction

High-entropy ceramics (HECs) are an emergent class of multicomponent ceramic materials possessing high ideal configurational entropy of mixing, ΔS_{mix} (>1.5k_B per cation on at least one sublattice in one definition for HECs) [1]. In most reported studies, HECs composing of five equimolar components, which result in ~1.6k_B per cation ideal ΔS_{mix} on one sublattice, were fabricated and investigated. HECs have attracted widespread attention because of their vast compositional design spaces and promising mechanical and other physical properties. Specifically, high-entropy oxides in the rock-salt [2], perovskite [3], fluorite [4], pyrochlore [5–8], weberite [9], bixbyite [10,11], and spinel [12] crystal structures have been studied. In addition, HECs have been expanded to include non-oxide systems, including high-entropy diborides [13] and other borides [14–17], silicides [18,19], carbides [20,21], nitrides [22,23], and carbonitrides [23,24] with mixed bonding, high-entropy fluorides [25–27] and sulfides [28,29] that are mostly ionic, and high-entropy aluminides that are mostly intermetallic [30]. In 2020, it was proposed to extend HECs to compositionally complex ceramics (CCCs), where non-equimolar compositions and short- and long-range ordering, which can reduce the configurational entropies, offer additional dimensions to tailor and improve materials properties [1,31].

Fluorite and fluorite-based oxides have broad technological applications. For example, Y_2O_3-stabilized ZrO_2 (YSZ) in the fluorite or related (tetragonal and metastable T') structures, as well as rare earth zirconates $RE_2Zr_2O_7$ in either the disordered defect fluorite structure or the ordered pyrochlore structure and rare earth niobates RE_3NbO_7 in either the disordered defect fluorite structure or the ordered weberite structure, are thermally insulating materials with applications in thermal barrier coatings (TBCs) [32–34]. Here, the base MO_2 fluorite structure ($Fm\bar{3}m$, *No.*225) is a cation-disordered cubic structure. The cubic $A_2B_2O_7$ pyrochlore structure ($Fd\bar{3}m$, *No.* 227) is a derivative of the fluorite structure with a $2 \times 2 \times 2$ supercell. In addition, fluorite can transform into the orthorhombic C_3DO_7 weberite structure ($C222_1$, *No.* 20), with a $\sim 2\times \sim \sqrt{2}\times \sim \sqrt{2}$ supercell. Phase transitions between the disordered fluorite structure and the ordered pyrochlore or weberite structure can affect their thermal and mechanical properties [5,35,36].

In 2018, Gild *et. al.* [4] reported the fabrication of eight single-phase, YSZ-like, high-entropy fluorite oxides, such as $(Zr_{1/5}Hf_{1/5}Ce_{1/5}Y_{1/5}Gd_{1/5})O_{2-\delta}$, which exhibit reduced thermal

* Corresponding author at: Aiiso Yufeng Li Family Department of Chemical and Nano Engineering, University of California San Diego, La Jolla, CA 92093, USA.
E-mail address: jluo@alum.mit.edu (J. Luo).

https://doi.org/10.1016/j.jeurceramsoc.2024.05.058
Received 14 March 2024; Received in revised form 18 May 2024; Accepted 21 May 2024
Available online 22 May 2024

conductivities. In 2020, Wright *et al.* further demonstrated that non-equimolar compositionally complex fluorite oxides can outperform their equimolar, higher-entropy counterparts [31]. Various high-entropy fluorite [37–43] (including rare earth zirconates [41] and niobates [42,43] in defect fluorite structure) and pyrochlore [40,44] oxides have been investigated for TBC applications. Wright *et al.* also showed that size disorder, instead of the configurational entropy, controls the reduced thermal conductivity in pyrochlore oxides [8]. In addition, the short-range weberite type ordering gives rise to the ultralow thermal conductivities of medium- and high-entropy rare earth niobates and tantalates [45]. Subsequently, a class of compositionally complex fluorite-based oxides (CCFBOs) with non-equimolar compositional designs [31,46–48], long- and short-range orders [8,31,36,45,47–49], and order-disorder transitions [5,35], including ultrahigh-entropy compositions with 10–21 components [9,35,36], have been fabricated and investigated. Researchers also fabricated and characterized fluorite-pyrochlore [50] and fluorite-bixbyite [10] dual-phase CCFBOs.

In this study, we designed a new series of 20-component CCFBOs with the general chemical formula $(15RE_{1/15})_{2x+1}(Ce_{1/3}Zr_{1/3}Hf_{1/3})_{3-3x}(Nb_{1/2}Ta_{1/2})_xO_{8-\delta}$ $(0 \le x \le 1)$, where "$15RE_{1/15}$" represents an equimolar mixture of 15 rare earth elements (La, Pr, Nd, Sm, Eu, Gd, Tb, Dy, Y, Ho, Er, Tm, Yb, Lu, and Sc). These CCFBOs were made by mixing the fluorite endmember $(15RE_{1/15})_1(Ce_{1/3}Hf_{1/3}Zr_{1/3})_3O_{7.5}$ and the weberite endmember $(15RE_{1/15})_3(Nb_{1/2}Ta_{1/2})_1O_7$. Here, the general chemical formula can also be rewritten as $[(15RE_{1/15})_1(Ce_{1/3}Hf_{1/3}Zr_{1/3})_3O_{7.5}]_{1-x}[(15RE_{1/15})_3(Nb_{1/2}Ta_{1/2})_1O_7]_x$, denoted as $20CCFBO_{x\mathrm{Nb/Ta}}$, where subscript "*x*Nb/Ta" represents the fraction of Nb/Ta-based weberite endmember. X-ray diffraction (XRD) shows that this series of $20CCFBO_{x\mathrm{Nb/Ta}}$ possess single ultrahigh-entropy phases, undergoing an abrupt fluorite-pyrochlore transition at $x = \sim 0.27$ and an abrupt pyrochlore-weberite transition at $x = \sim 0.87$ with increasing compositional variable x.

2. Experimental procedure

2.1. Composition design

We designed and fabricated this series of $20CCFBO_{x\mathrm{Nb/Ta}}$ by mixing single-phase fluorite endmember F1 $(15RE_{1/15})_1(Ce_{1/3}Hf_{1/3}Zr_{1/3})_3O_{7.5}$ with single-phase weberite endmember W17 $(15RE_{1/15})_3(Nb_{1/2}Ta_{1/2})_1O_7$ in different fractions to form $F1_{1-x}W17_x$, where $x = 0$, 0.25, 0.2656, 0.2734, 0.2813, 0.3125, 0.375, 0.5, 0.75, 0.8125, 0.8438, 0.8594, 0.8672, 0.875, 0.9063, 0.9375, and 1, respectively.

2.2. Materials and synthesis

We first prepared three mixtures of $(15RE_{1/15})_2O_3$, $(Ce_{1/3}Hf_{1/3}Zr_{1/3})O_2$, and $(Nb_{1/2}Ta_{1/2})_2O_5$, each of which were made by using commercially available high-purity binary oxide (La_2O_3, Pr_6O_{11}, Nd_2O_3 Sm_2O_3, Eu_2O_3, Gd_2O_3, Tb_4O_7, Dy_2O_3, Y_2O_3, Ho_2O_3, Er_2O_3, Tm_2O_3, Yb_2O_3, Lu_2O_3, Sc_2O_3, CeO_2, ZrO_2, HfO_2, Nb_2O_5, and Ta_2O_5) powders obtained from US Research Nanomaterials, TX, USA, with a particle size of ~ 5 μm and a purity > 99%. For each mixture, a batch of 10 g powders was weighted in appropriate proportions and placed into a 100 mL YSZ ball mill jar. A ball-to-powder ratio of 10:1 was used, along with an appropriate amount of isopropyl alcohol (IPA) to form slurries. A planetary ball mill (PQN04 gear-drive mill from Across International LLC, USA) was used to mix and mill the powders at a rotation speed of 300 rpm for 24 h for homogenization. Subsequently, the milled mixtures were dried overnight at 75 °C in an oven.

To fabricate the targeted $20CCFBO_{x\mathrm{Nb/Ta}}$ compositions, the milled mixtures were weighed in a 2 g batch following the designed stoichiometry. The batches were then placed in a poly (methyl methacrylate) high-energy ball mill (HEBM) vial with two tungsten carbide (WC) inserts and a Ø 5/16" (~ 7.94 mm) WC ball. Approximately 1 wt% stearic acid was introduced as the process control agent. Consequently, the vials were placed in a SPEX 8000D mill (SPEXCertPrep, NJ, USA) and HEBM for 100 min. The as-milled powders were pressed into green pellets under a pressure of approximately 100 MPa using a hydraulic press. Then, the green pellets were placed on a Pt foil in an alumina crucible and sintered in a high-temperature box furnace (SentroTech, OH, USA) at 1600 °C for 24 h with a ramping rate of 5 °C/min, followed by furnace cooling. The sintered pellets were ground and polished for further characterization.

2.3. Characterization

2.3.1. X-ray diffraction (XRD)

X-ray diffraction (XRD) patterns were acquired using a Rigaku Miniflex II diffractometer operating at 30 kV and 15 mA, in a continuous scan mode with Cu Kα radiation. The full XRD patterns were obtained with a step size of 0.02 ° and a scan speed of 2.3 °/min. Slow scans were conducted to measure characteristic peaks at specific 2θ degree ranges, using a step size of 0.005 ° and a scan speed of 0.2 °/min. For compositions near the transition points, the slowest scan speed of 0.1 °/min was employed. The lattice parameters were obtained by unit cell refinements using the JADE software.

2.3.2. Scanning electron microscopy (SEM)

Scanning electron microscopy (SEM), electron dispersive X-ray spectroscopy (EDS), and electron backscatter diffraction (EBSD) analysis were carried out using a ThermoFisher (Formerly FEI) Apreo microscope equipped with an Oxford N-Max^N EDX detector at an acceleration voltage of 20 kV to examine the microstructure, compositional homogeneity, and grain size. For grain size measurements, the number of grains counted in each EBSD image exceeds 10,000 to ensure statistically reliable data.

2.3.3. Young's modules (*E*)

The bulk densities ρ of each specimen were measured abiding the ASTM Standard C373–18. At the same time, the relative density was also assessed through digital image processing of porosity on cross-sectional SEM images. All specimens possess high relative densities of > 98%. Young's modulus (E) measurement was conducted in a Tektronix TDS 420 A digital oscilloscope following the ASTM Standard C1198–20. For each specimen, the longitudinal (u_L) and transverse (u_T) wave speeds were measured > 3 times at different locations. Poisson's ratio (ν) and measured Young's modulus were determined from Eqs. (1) and (2):

$$\nu = \frac{u_L^2 - 2u_T^2}{2(u_L^2 - u_T^2)} \tag{1}$$

$$E_{measured} = 2u_T^2\rho(1+\nu) \tag{2}$$

Then, Young's modulus was corrected for porosity using the following equation [51]:

$$E = \frac{E_{measured}}{1 - 1.29P}, \tag{3}$$

where P is the porosity.

2.3.4. Thermal conductivity (*k*)

The thermal conductivity (k) of the specimens at 200 °C was measured by modulated photothermal radiometry (MPR). MPR is a non-contact frequency-domain thermal characterization technique for high-temperature bulk solids and liquids [52,53]. Upon measurement, the specimen was heated by an intensity-modulated laser with an angular frequency ω. The surface temperature oscillation of the specimen ($|\theta_s|$) was recorded by both an infrared (IR) detector and a pyrometer. From the slope of $|\theta_s|$ *vs.* $\omega^{-\frac{1}{2}}$, the thermal effusivity ($e_{measured}$) of the specimen can be obtained. The measured thermal effusivity $e_{measured}$ of a bulk solid

can be converted to the measured thermal conductivity $k_{measured}$ using the following relation [52]:

$$k_{measured} = \frac{{e_{measured}}^2}{\rho c_P}, \quad (4)$$

where ρ is the measured density of the specimen. The Neumann-Kopp rule was used to estimate the specific heat capacity (c_P) through mixing the heat capacity value of constituent binary oxides according to specific stoichiometry [54]. Then, the thermal conductivity was corrected for porosity by the following Equation:

$$k = \frac{k_{measured}}{(1-P)^{3/2}} \quad (5)$$

where k is the bulk thermal conductivity with porosity (P) correction. Typically, the measurement uncertainty in thermal conductivity using MPR is around 10%.

3. Results and discussion

3.1. Formation of ultrahigh-entropy phases

The sample ID, measured density, relative density, lattice parameters, grain sizes, Young's modulus, porosity, and thermal conductivities of all 17 specimens are summarized in Table 1. Fig. 1(a) illustrates a schematic of the phase formation in this series of 20CCFBO$_{x\text{Nb/Ta}}$ compositions, which form single fluorite, pyrochlore, and weberite ultrahigh-entropy phases based on XRD characterization (albeit < 1 vol % secondary phases were identified by high-resolution SEM-EDS analyses in two compositions near the two phase-transition points without detectable XRD peaks).

As shown in Table 1, all 17 specimens were sintered to > 98% relative densities (and 14 of them are > 99% relative densities) using the densities measured by Archimedes methods and theoretical densities calculated from XRD-measured lattice parameters. The high relative densities were also independently confirmed by measured porosity from SEM images, which showed that the porosity is < 1% for 14 specimens and < 2% for all 17 specimens (Table 1).

The endmember F1 $(15RE_{1/15})_1(Ce_{1/3}Zr_{1/3}Hf_{1/3})_3O_{7.5}$ is in the disordered $MO_{2-\delta}$ fluorite structure ($Fm\bar{3}m, No.225$) and the endmember W17 $(15RE_{1/15})_3(Nb_{1/2}Ta_{1/2})_1O_7$ is in orthorhombic weberite C_3DO_7 structure ($C222_1, No.$ 20). Both XRD and EDS elemental mapping (Suppl. Figs. S1 and S17 in *Appendix A:* Supplementary Data) indicate these two endmembers are compositionally homogeneous single phases without detectable secondary phases. When endmembers F1 and W17 were mixed in designed fractions $F1_{1-x}W17_x$ ($0 \le x \le 1$), 20CCFBO$_{x\text{Nb/Ta}}$ exhibits phase transition with increasing compositional variable x from fluorite ($Fm\bar{3}m, No.225$) to $A_2B_2O_7$ pyrochlore ($Fd\bar{3}m, No.$ 227) and then

Table 1
The measured density, relative density, lattice parameter, grain size, Young's modulus (E), and thermal conductivity k for the 17 specimens in the series of 20CCFBO$_{x\text{Nb/Ta}}$ ($0 \le x \le 1$) with the chemical formula $[(15RE_{1/15})_1(Ce_{1/3}Hf_{1/3}Zr_{1/3})_3O_{7.5}]_{1-x}[(15RE_{1/15})_3(Nb_{1/2}Ta_{1/2})_1O_7]_x$. Standard deviations are represented by the ± values in the table.

ID	x	Density (g/cm^3)	Relative Density	Lattice Parameter (Å)			Grain Size (μm)	Youngs' Modulus (GPa)	Thermal Conductivity (W·m^{-1}·K^{-1})
				a_F, $1/2a_P$, or $1/2a_W$	$1/\sqrt{2}b_W$	$1/\sqrt{2}c_W$			
W17	1	7.61	0.99	5.2696 ± 0.0005	5.2607 ± 0.0030	5.3129 ± 0.0015	4.96 ± 1.99	227.87 ± 1.73	1.3272 ± 0.1327
W16	0.9375	7.59	0.99	5.2739 ± 0.0021	5.3075 ± 0.0017	5.2680 ± 0.0041	2.73 ± 0.75	245.19 ± 5.19	1.2513 ± 0.1251
W15	0.9063	7.63	1.00	5.2716 ± 0.0014	5.2597 ± 0.0007	5.2993 ± 0.0004	3.76 ± 1.33	243.12 ± 1.97	1.1540 ± 0.1154
W14	0.875	7.61	0.99	5.2693 ± 0.0007	5.2588 ± 0.0064	5.2946 ± 0.0018	4.10 ± 1.50	234.19 ± 5.48	1.2822 ± 0.1282
P_W13	0.8672	7.65	0.99	5.2815 ± 0.0010			10.52 ± 4.72	229.96 ± 5.24	1.1889 ± 0.1189
P_W12	0.8594	7.62	0.98	5.2799 ± 0.0006			6.78 ± 2.91	230.08 ± 5.53	1.1660 ± 0.1166
P_W11	0.8438	7.60	0.99	5.2799 ± 0.0006			5.61 ± 2.36	240.06 ± 3.83	1.1532 ± 0.1153
P10	0.8125	7.63	0.99	5.2761 ± 0.0001			6.60 ± 2.75	224.09 ± 0.83	1.3402 ± 0.1340
P9	0.75	7.60	0.99	5.2752 ± 0.0000			7.43 ± 3.16	227.27 ± 3.68	1.4450 ± 0.1445
P8	0.5	7.69	0.99	5.2650 ± 0.0003			6.22 ± 2.62	238.37 ± 1.77	1.2799 ± 0.1280
P7	0.375	7.67	0.99	5.2624 ± 0.0010			3.85 ± 1.37	258.12 ± 8.51	1.5718 ± 0.1572
P6	0.3125	7.63	1.00	5.2556 ± 0.0003			4.73 ± 1.90	244.70 ± 2.09	1.3886 ± 0.1389
P5	0.2813	7.66	0.99	5.2581 ± 0.0010			7.16 ± 3.23	245.45 ± 4.48	1.3320 ± 0.1332
P4	0.2734	7.56	0.99	5.2552 ± 0.0002			7.12 ± 3.45	246.24 ± 4.46	1.4931 ± 0.1493
P3	0.2656	7.66	1.00	5.2545 ± 0.0005			7.13 ± 3.25	236.91 ± 5.00	1.5311 ± 0.1531
F2	0.25	7.48	0.99	5.2512 ± 0.0046			20.32 ± 8.55	230.59 ± 2.51	1.5154 ± 0.1515
F1	0	7.32	0.98	5.2425 ± 0.0004			34.56 ± 18.53	221.64 ± 1.39	1.4817 ± 0.1482

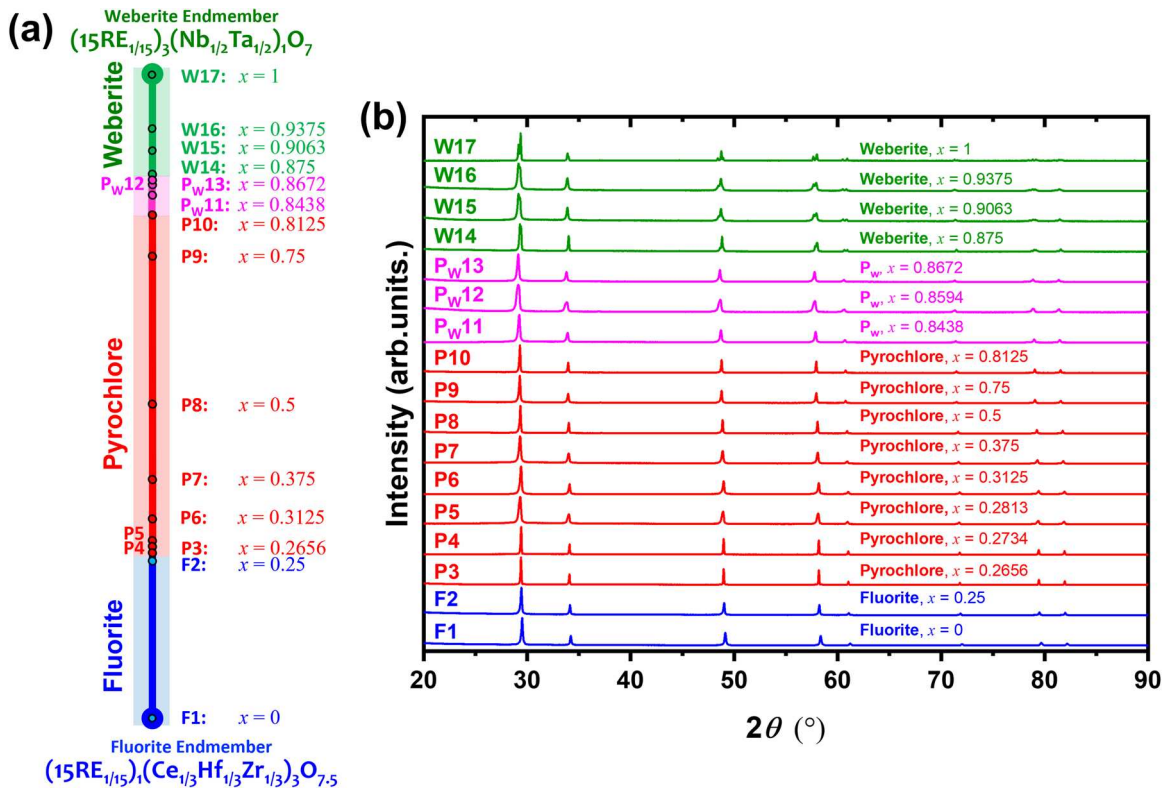

Fig. 1. (a) Schematic illustration of the phase transitions in a series of 20-component fluorite-based compositionally complex oxides (20CCFBOs) fabricated and investigated in this study. The endmember F1, $(15RE_{1/15})_1(Ce_{1/3}Hf_{1/3}Zr_{1/3})_3O_{7.5}$, possesses a single-phase cubic fluorite structure, where "$15RE_{1/15}$" represents $La_{1/15}Pr_{1/15}Nd_{1/15}Sm_{1/15}Eu_{1/15}Gd_{1/15}Tb_{1/15}Dy_{1/15}Y_{1/15}Ho_{1/15}Er_{1/15}Tm_{1/15}Yb_{1/15}Lu_{1/15}Sc_{1/15}$. The other endmember W17, $(15RE_{1/15})_3(Nb_{1/2}Ta_{1/2})_1O_7$, adopts the single-phase orthorhombic weberite structure. When the endmembers F1 and W17 are mixed in the designed fractions ($F1_{1-x}W17_x$, $0 \le x \le 1$), a series of 20CCFBOs with the compositions $(15RE_{1/15})_{2x+1}(Ce_{1/3}Zr_{1/3}Hf_{1/3})_{3-3x}(Nb_{1/2}Ta_{1/2})_xO_{8-\delta} = [(15RE_{1/15})_1(Ce_{1/3}Hf_{1/3}Zr_{1/3})_3O_{8-\delta}]_{1-x}[(15RE_{1/15})_3(Nb_{1/2}Ta_{1/2})_1O_7]_x$ form virtually single ultrahigh-entropy phases in the MO_2 fluorite (F, $0 \le x \le 0.25$), $A_2B_2O_7$ pyrochlore (P, $0.2656 \le x \le 0.8672$), or C_3DO_7 weberite (W, $0.875 \le x \le 1$) structure for 17 specimens: F1, F2, P3, P4, P5, P6, P7, P8, P9, P10, P_W11, P_W12, P_W13, W14, W15, W16, and W17. Here, "F", "P", or "W" represents the phase determined by XRD (for their long-range crystal ordering), and "P_W" refers to possible short-range weberite (W) ordering in the long-range pyrochlore (P) phase in specimens P_W11-P_W13. (b) XRD patterns of these 17 specimens in the 20CCFBO series in single-phase fluorite ($Fm\bar{3}m$, No. 225), pyrochlore ($Fd\bar{3}m$, No. 227), or weberite ($C222_1$, No. 20) structure, with no secondary phase detectable by XRD. XRD peaks are indexed in Fig. 2 and Fig. 4 in expanded views.

C_3DO_7 weberite ($C222_1$, *No.* 20) for these 17 specimens. All 17 specimens exhibit single phases in the XRD patterns with no detectable peaks for secondary phases (Fig. 1(b)).

The microstructures of these 17 specimens are carefully examined under SEM and EDS mapping at different areas and higher magnifications to characterize compositional homogeneity and identify any secondary phase undetectable by XRD. This series of 17 $20CCFBO_{xNb/Ta}$ specimens are compositionally homogeneous according to EDS mapping results (Suppl. Fig. S1–S17), except for <1 vol% secondary phases in specimens F2 and P_W13 (Suppl. Figs. S2, S13, and S18), which represent the compositions before the fluorite-pyrochlore and pyrochlore-weberite phase transitions, respectively.

To quantify the volume fractions of secondary phases in specimens F2 and P_W13, more than 10 SEM images were randomly acquired for F2 and P_W13 at high magnifications. Subsequently, the volume fractions of secondary phases were determined based on cross-sectional SEM images to be < 1 vol% in both cases. EDS elemental analysis further revealed that both secondary phases were enriched in large cations such as Pr^{3+} and depleted in small cations such as Zr^{4+}, Hf^{4+}, Nb^{5+}, and Ta^{5+}, as shown in Suppl. Fig. S18(c). EDS-mapping results, illustrating individual cation distribution in F2 and P_W13, are presented in Suppl. Figs. S2 and S13. On the one hand, the Gibbs phase rule suggests that up to 20 phases can coexist at thermodynamic equilibrium in a 20-component system. Interestingly, our experiment observations reveal the presence of only one minor secondary phase (< 1 vol%) near both phase transition points. A similar abrupt phase transition was also reported in a few other ultrahigh-entropy CCFBOs [7,29,48]. The observed abrupt transition (or narrow multi-phase regions) may be due to the high configurational entropy, but the exact underlying reason is still elusive and should be further investigated in a future study. It is reasonable that the (minor) secondary phases are enriched in large cations such as Pr^{3+}, which have the largest size misfit in the primary phases.

3.2. *The fluorite-pyrochlore transition*

Indexed XRD patterns for the fluorite-pyrochlore transition are shown in Fig. 2. Note that the lattice parameter of the pyrochlore phase is twice that of the fluorite phase. For example, the fluorite $(200)_P$ peak corresponds to the pyrochlore $(400)_P$ peak. To meticulously examine the fluorite-pyrochlore transition, slow-scan XRD was conducted for 2θ angle range encompassing the characteristic pyrochlore superstructure $(331)_P$ peak at $2\theta = 36.5 \sim 38°$ (Fig. 2(b)). As shown in Fig. 2(b), the pyrochlore $(331)_P$ superstructure peak gradually broadened with reduced intensity from specimen P6 to specimen P3 and disappeared in specimens F2 and F1.

To further explore characteristic peak changes with varying x, the normalized pyrochlore $(331)_P$ intensity (represented by the ratio of integrated peak intensity for $(331)_P$ *vs.* $(400)_P$ peaks) and full width at half maximum (FWHM) of the characteristic pyrochlore superstructure $(331)_P$ peak were extracted from the peak fittings and plotted in Fig. 3(a) and Fig. 3(b), respectively, as the order parameters for the (pyrochlore-fluorite) order-disorder transition (ODT). As shown in Fig. 3(a), the

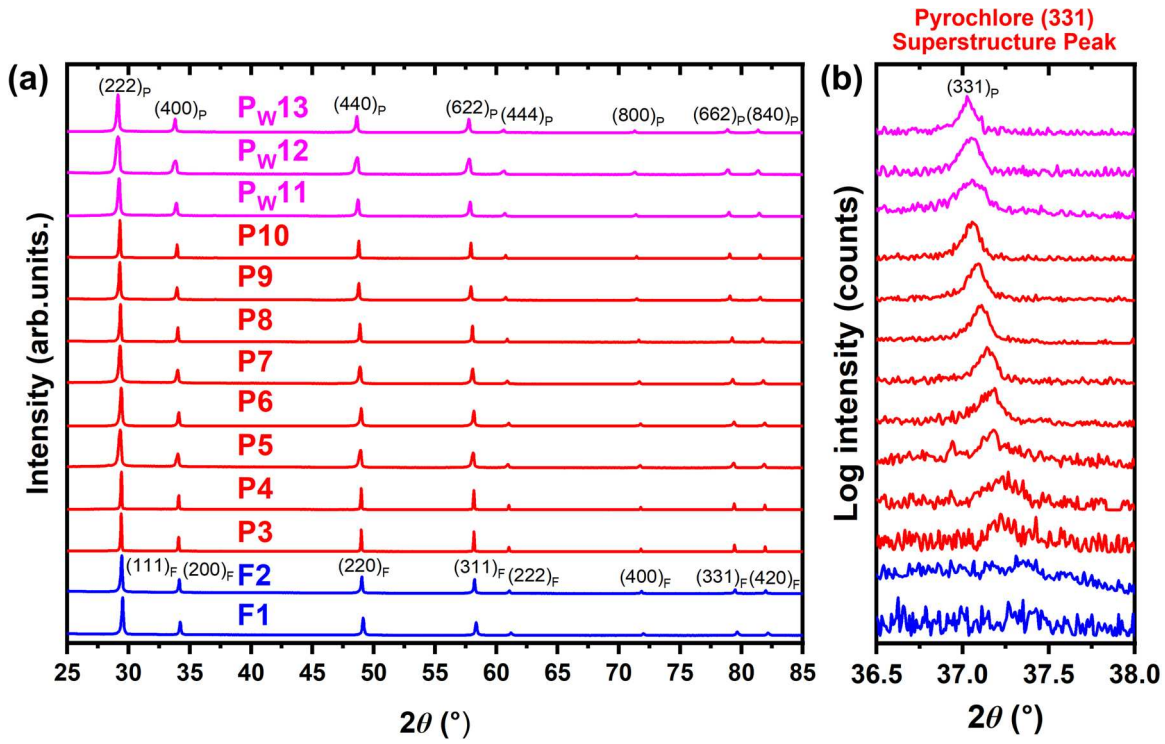

Fig. 2. (a) The evolution of XRD patterns showing a fluorite-pyrochlore transition. (b) Logarithmic intensity plots showing the disappearance of the characteristic pyrochlore superstructure peak $(331)_P$ between F2 ($x = 0.25$) and P3 ($x = 0.2656$).

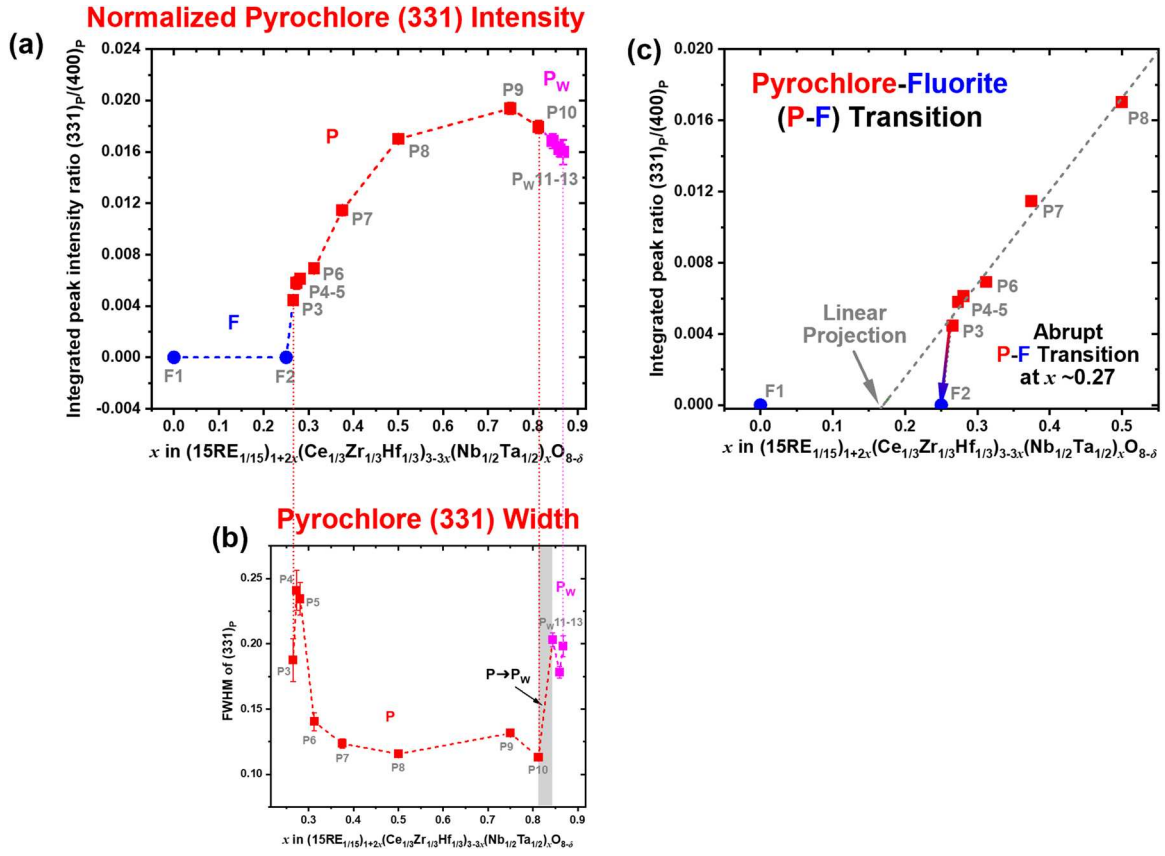

Fig. 3. (a) The evolution of normalized pyrochlore $(331)_P$ intensity with varying compositional variable x ($0 \leq x \leq 0.8672$) during the fluorite-pyrochlore transition. (b) The corresponding evolution of the pyrochlore $(331)_P$ peak width, full width at half maximum (FWHM), with x. (c) Enlarged view of the fluorite-pyrochlore transition with a linear projection of the peak intensity. The actual pyrochlore-to-fluorite order-disorder transition (ODT) is more abrupt.

normalized pyrochlore $(331)_P$ intensity increases from P3, peaks at P9, and then gradually declines until P_W13. The corresponding FWHM of pyrochlore $(331)_P$ peaks undergoes a transition from wide (P3-P5) to sharp (P6-P10), followed by broadening again (P_W11-P_W13), as shown in Fig. 3(b). This observation suggests a structural fluctuation of the pyrochlore phase in specimens P3-P5 as the fluorite phase transits to the ordered pyrochlore phase. In other words, specimens P3-P5 (right after the occurrence of the fluorite-pyrochlore transition) are likely not perfectly ordered. With further increasing compositional variable x, the pyrochlore order gradually improved (P6-P8) and reached its peak at P9 ($x = 0.75$), as indicated by enhanced normalized peak intensity and decreased FWHM of the pyrochlore characteristic $(331)_P$ peak in Fig. 3 (b).

Fig. 3(c) shows an enlarged view of the pyrochlore-fluorite ODT region. A linear projection was employed to predict the fluorite-pyrochlore phase transition point using six data points (P3-P8, $x =$ 0.2656, 0.2734, 0.2813, 0.3125, 0.375, 0.5) right after the observed phase transition. The linear regression produced: $y = -0.00887 + 0.06226x$, $R^2 = 0.9875$. This suggested a projected pyrochlore-fluorite order-disorder transition (ODT) at $x = 0.1697 \pm 0.0193$. However, the experimental observed ODT took place at $x \approx 0.27$, which indicated a more abrupt phase transition (ODT) as indicated by the characteristic pyrochlore $(331)_P$ peak (Fig. 3(c)).

3.3. The pyrochlore-weberite transition

Moreover, Fig. 3(a) shows that the intensity of the characteristic pyrochlore $(331)_P$ peak gradually reduced again from P10 ($x = 0.8125$) to P_W13 ($x = 0.8672$), while the peak significantly broadened in P_W11 ($x = 0.8438$) to P_W13 ($x = 0.8672$) as it approaches the weberite phase region. This may be ascribed to the possible emergence of short-range weberite ordering (as discussed later).

To show the pyrochlore-weberite transition, enlarged views of XRD patterns of the peak splitting due to the reduction in symmetry from the cubic pyrochlore phase to the orthorhombic weberite phase are shown in Fig. 4. Here, the most distinct signature of the cubic pyrochlore to the orthorhombic weberite phase transition is represented by the splitting of the pyrochlore $(444)_P$ peak to weberite $(404)_W$ and $(440)_W$ peaks, as shown Fig. 4(c) at $2\theta = 59 \sim 62°$.

The peak splitting ($\Delta 2\theta$) and associated peak broadening (in FWHM) during the pyrochlore-weberite transition were analyzed in detail in Fig. 5(a) using peak fitting data. As illustrated in Fig. 5(a), pyrochlore $(444)_P$ remained almost unchanged in specimens P9 ($x = 0.75$) and P10 ($x = 0.8125$) until peak broadening became noticeable in specimen P_W11 ($x = 0.8438$). As compositional variable x further increased, pyrochlore $(444)_P$ continues to broaden until reaches its maximum at specimen P_W13 ($x = 0.8672$). Subsequently, peak splitting (from the pyrochlore $(444)_P$ to weberite $(404)_W$ and $(440)_W$) took place and $\Delta 2\theta$ increased from W14 ($x = 0.875$) to W17 ($x = 1$). The peak splitting was accompanied by increased intensity of the split weberite peaks $(404)_W$ and $(440)_W$, indicating increasing weberite ordering with increasing x.

As an interesting observation, even though the XRD showed that specimens P_W11- P_W13 were still in the pyrochlore phase for their long-range ordering (Fig. 3(c)), the gradual $(444)_P$ peak broadening in P_W11-P_W13 suggested the possible emergence of short-range weberite ordering.

Similarly, for the pyrochlore-fluorite ODT, a linear regression was employed to predict the pyrochlore-weberite phase transition using four $\Delta 2\theta$ data for W14-W17 ($x = 0.875$, 0.9063, 0.9375, and 1), producing: $y = -1.0246 + 1.48091x$, $R^2 = 0.9477$. The projected pyrochlore-weberite phase transition was at $x = 0.6919 \pm 0.1546$. However, the experimentally observed pyrochlore-weberite phase transition took place between $x = 0.8672$ and $x = 0.875$ (as shown in enlarged Fig. 5 (b)), indicating a more abrupt weberite-to-pyrochlore transition.

3.4. Discussion of phase stability and descriptors

To understand phase stability and evolution, we define and evaluate several descriptors. In these calculations, we assume that 3+ cations prefer to occupy the A-site, while 4+ cations show a preference for the B-site in $A_2B_2O_7$ pyrochlore (like their typical ternary pyrochlores). Similarly, 3+ cations will prefer the C-site and 5+ cations will prefer the D-site in C_3DO_7. Next, we assume that larger cations would prefer to occupy the A- or C-site, while smaller cations would prefer to occupy the B- or D-site, in $A_2B_2O_7$ pyrochlore and C_3DO_7 weberite phases, respectively.

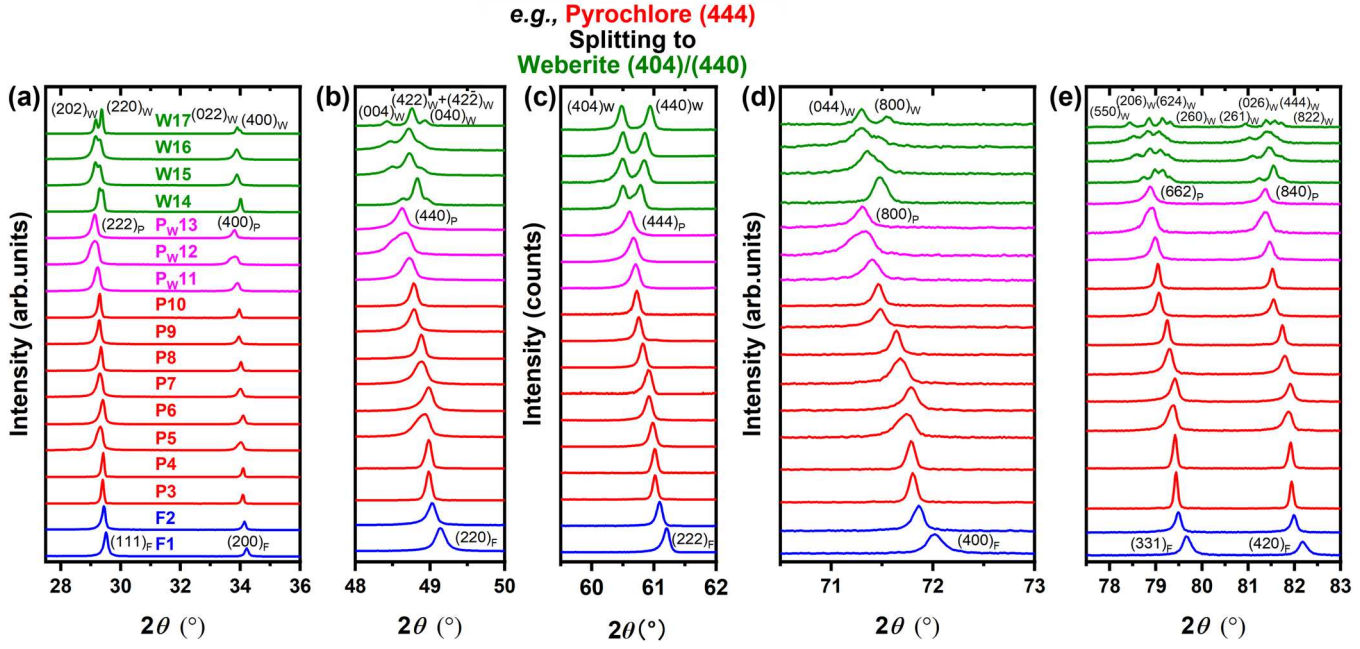

Fig. 4. Enlarged views showing the evolution of XRD peaks from fluorite to pyrochlore to weberite phases in selected regions, with indexed XRD peaks. The most distinct signature of the cubic pyrochlore to the orthorhombic weberite phase transition is represented by the splitting of the pyrochlore $(444)_P$ peak to weberite $(404)_W$ and $(440)_W$ peaks, as shown in panel (c).

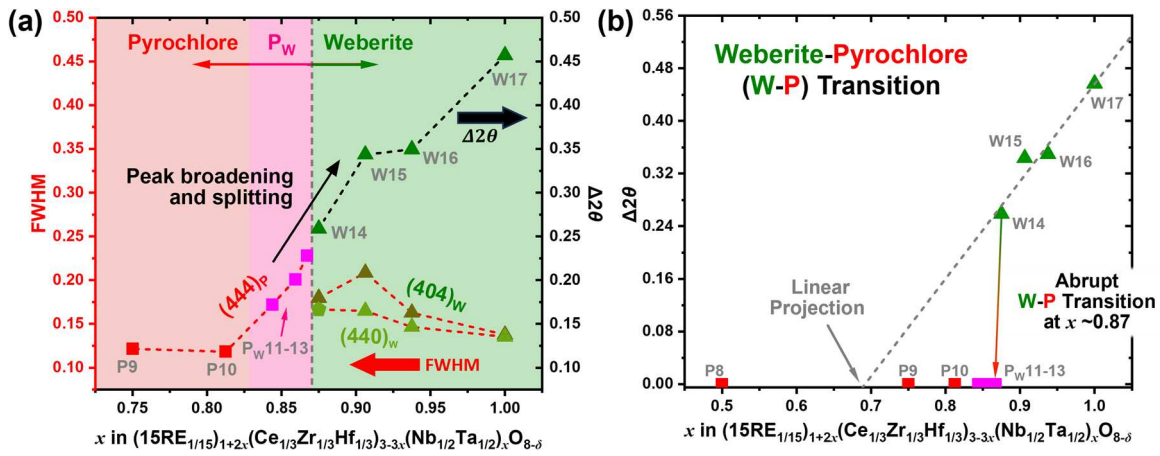

Fig. 5. (a) The evolution of the full width at half maximum (FWHM) and weberite peak splits ($\Delta 2\theta$) *vs.* varying compositional variable x ($0.75 \le x \le 1$) during the pyrochlore-weberite transition. (b) An enlarged view of the pyrochlore-weberite transition, which is more abrupt than the projection from linear extrapolation of the weberite peak splits.

First, we computed and plotted ideal configurational entropies of mixing *vs.* compositional variable x in Fig. 6. For the pyrochlore and weberite phases with two sublattices, we computed and plotted the mixing entropy for each sublattice. Then, we plotted weighted average entropies using the following formula: $\overline{\Delta S_P^{mix}} \equiv \frac{1}{2}\Delta S_{A\ site}^{mix} + \frac{1}{2}\Delta S_{B\ site}^{mix}$ for the $A_2B_2O_7$ pyrochlore phase and $\overline{\Delta S_W^{mix}} \equiv \frac{3}{4}\Delta S_{C\ site}^{mix} + \frac{1}{4}\Delta S_{D\ site}^{mix}$ for the C_3DO_7 weberite phase. The computed weighted average ideal configurational entropies of mixing are generally greater than $2k_B$ per cation in this series of 17 20CCFBO$_{x\mathrm{Nb/Ta}}$ compositions, which indicates that this series of 20CCFBOs are ultrahigh-entropy phases [9]. The actual configurational entropies can be reduced with short-range ordering. There is no apparent relationship between configurational entropies and phase formation and transition.

Next, we used Shannon radii [55] to calculate several descriptors to analyze phase formation and stability. We calculated the averaged cation radii ratio $\overline{r_A}/\overline{r_B}$ for the $A_2B_2O_7$ pyrochlore structure for both P3-P_W13 (that were stable in the pyrochlore phase) and F1 and F2 (that were assumed to be metastable pyrochlore phase, despite that they formed stable fluorite phase) and plotted $\overline{r_A}/\overline{r_B}$ *vs.* x in Fig. 7(a). For pyrochlore, the A-site cations are 8-coordinated, and the B-site cations are 6-coordinated; thus, the Shannon radii [55] were selected based on the coordination numbers.

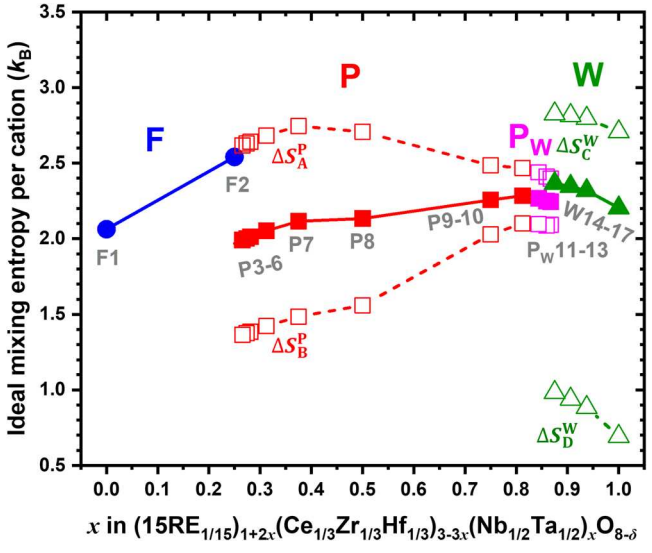

Fig. 6. Computed ideal configurational entropy of mixing (in the unit of k_B per cation) *vs.* compositional variable x. For the pyrochlore and weberite phases with two sublattices, the solid data points, and solid lines represent the weighted average configurational entropy, and the hollow data points and dashed lines represent the configurational entropies on each sublattice. The weighted average configurational entropies are defined as: $\overline{\Delta S_P^{mix}} \equiv \frac{1}{2}\Delta S_{A\ site}^{mix} + \frac{1}{2}\Delta S_{B\ site}^{mix}$ for the $A_2B_2O_7$ pyrochlore phase and $\overline{\Delta S_W^{mix}} \equiv \frac{3}{4}\Delta S_{C\ site}^{mix} + \frac{1}{4}\Delta S_{D\ site}^{mix}$ for the C_3DO_7 weberite phase.

Prior studies suggested pyrochlore structure forms when $\overline{r_A}/\overline{r_B} >\sim 1.46$ in ternary $A_2B_2O_7$ oxides. However, the pyrochlore-fluorite ODT took place between P3 ($x = 0.2656$) and F2 ($x = 0.25$) with a lower threshold of $\overline{r_A}/\overline{r_B} \approx 1.405$. The shifted ODT thresholds were previously reported in other CCFBOs. In 11-component CCFBOs (that are duodenary oxides, including O), an ODT was found to occur at a higher threshold of $\overline{r_A}/\overline{r_B} \approx 1.48$ [5], while in another 10-component CCFBOs, the ODT occurred at a lower threshold of $\overline{r_A}/\overline{r_B} \approx 1.39$[29].

We notice that $\overline{r_A}/\overline{r_B}$ is almost a constant for F1 to P8 (as it varies slightly from ~1.0402 to ~1.0408). Thus, we believe that the $\overline{r_A}/\overline{r_B}$ ratio is not a good descriptor for predicting the ODT between F2 ($\overline{r_A}/\overline{r_B}$ = ~1.4051) and P3 ($\overline{r_A}/\overline{r_B}$ = ~1.4053) in this case. For F1 to P8, all rare earth cations can be accommodated at 8-coordinated A sites. A rather small jump in the $\overline{r_A}/\overline{r_B}$ ratio from P8 (~1.41) to P9 (~1.44) occurs when relative small rare earth cations Sc^{3+}, Lu^{3+}, and Yb^{3+} are forced to move to the unfavorable B sites, along with the final 12.5% of Ce^{4+} on the 8-coordinated A sites being moved to favorable B sites, where the Shannon radii are smaller with the coordination number of 6. Consequently, $\overline{r_A}$ reduces slightly from ~0.735 Å for P8 to ~ 0.734 Å for P9, while $\overline{r_B}$ increases from ~1.035 Å for P8 to ~ 1.058 Å for P9. We should note that this site occupation only represents an ideal scenario of cation distribution on A *vs.* B sites (as well as ignoring the possible valence variation for certain cations such as Ce).

Notably, P9 marks the highest normalized pyrochlore superstructure $(331)_P$ peak intensity among all pyrochlore specimens (Fig. 3(a)), coinciding with the largest $\overline{r_A}/\overline{r_B}$ ratio (Fig. 7(a)). Subsequently, a slight decreasing trend in $\overline{r_A}/\overline{r_B}$ is evident from P9 to P_W13 ($0.75 \le x \le 0.8672$), with an increasing amount of RE^{3+} cations being forced to move from the preferred A sites to the unfavorite B sites (ideally to be occupied by 4+ cations), along with more (non-ideal) 5+ cations on B sites. This observation coincides with a gradual occurrence of disordering (Fig. 3), with emergence of short-range $C222_1$ weberite ordering in the long-range pyrochlore-ordered phase.

We also calculated the averaged cation radii ratio, $\overline{r_C}/\overline{r_D}$, in the C_3DO_7 weberite phases for W14-W17 as well as P_W12 and P_W13 (assuming they are in the metastable weberite structure). In weberite coordination environment, the C sites include both 8-coordination (4*b*) and 7-coordination (8*c*), while the D-site is 6-coordination (4*b*). Due to

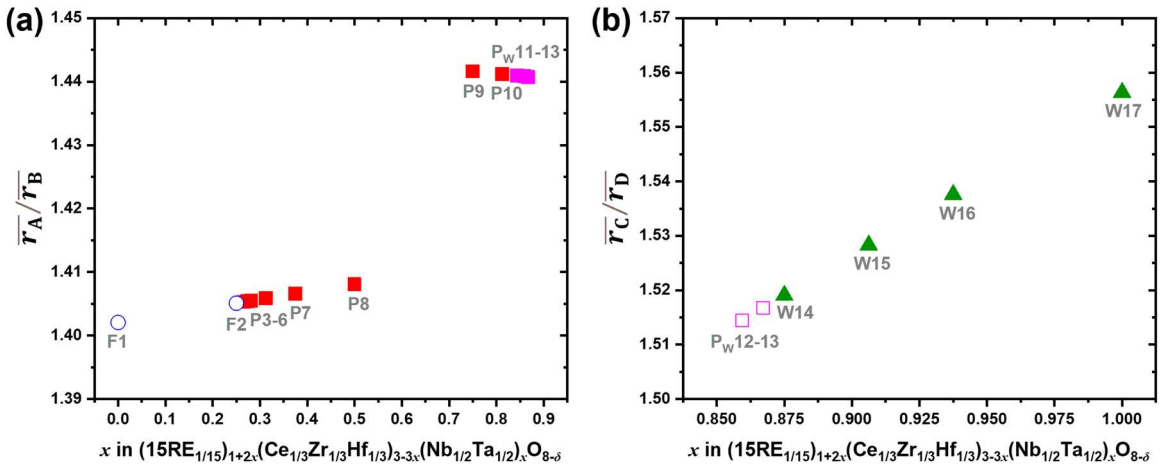

Fig. 7. The averaged cation radii ratio (a) $\overline{r_A}/\overline{r_B}$ and (b) $\overline{r_C}/\overline{r_D}$ *vs.* compositional variable x in this series of 20CCFBO$_{x\mathrm{Nb/Ta}}$ ($0 \le x \le 1$). The solid data points represent the calculated $\overline{r_A}/\overline{r_B}$ ratios for the stable pyrochlore phases and $\overline{r_C}/\overline{r_D}$ ratios for the stable weberite phases, respectively. The hollow data points in panel (a) represent the calculated $\overline{r_A}/\overline{r_B}$ ratios for compositions F1 and F2 if they were in the (unstable) $A_2B_2O_7$ pyrochlore structure (while they are in fact stable in the fluorite structure). Here, the fluorite-to-pyrochlore transition takes place at a threshold of $\overline{r_A}/\overline{r_B} \approx 1.405$ in this 20CCFBO$_{x\mathrm{Nb/Ta}}$ series. The hollow data points in panel (b) represent the calculated $\overline{r_C}/\overline{r_D}$ ratios for compositions P$_W$12–P$_W$13 if they were in the (unstable) C_3DO_7 weberite structure (while they are in fact stable in the pyrochlore structure for their long-range ordering). Here, the weberite-to-pyrochlore transition takes place at a threshold of $\overline{r_C}/\overline{r_D} \approx 1.52$ in this 20CCFBO$_{x\mathrm{Nb/Ta}}$ series.

limited data for cations of coordination number of 7 in Shannon radii, averaged cation radii of 8 coordination and 6 coordination are adopted for 7-coordinated cations. The results are shown in Fig. 7(b) as pink hollow data points for P$_W$ phases (metastable weberite phases) and green solid data points for weberite phases.

Prior studies indicate that weberite phases are stable when $\overline{r_{C^{3+}}}/\overline{r_{D^{5+}}} \ge 1.53$ in RE_3TaO_7 ternary oxides [56]. In this 20-component system, weberite phases stable at $\overline{r_C}/\overline{r_D} \ge 1.52$ (W14, $x = 0.875$, $(15RE_{0.0611}Ce_{0.0417}Zr_{0.0417})_2(Hf_{0.125}Nb_{0.4375}Ta_{0.4375})_2O_{8-\delta}$), exhibiting a threshold similar to ternary systems.

The $\overline{r_C}/\overline{r_D}$ ratio rises as x increases for $0.875 \le x \le 1$, which correlates with enhanced crystallinity in the weberite phase. This correlation is evidenced by the distinct peak splitting of pyrochlore $(444)_P$ peak into weberite $(440)_W$ and $(404)_W$ peaks for specimen W14-W17 (Fig. 5(a)). The crystallinity of weberite reaches its peak at W17 ($x = 1$, $(15RE_{1/15})_3(Nb_{1/2}Ta_{1/2})O_{8-\delta}$), where all 3+ rare earth cations occupy the C sites, and 5+ transition metal cations occupy the D sites (without anti-site cations), thereby being perfect for the C_3DO_7 weberite structure.

Fig. 8 illustrates the mean cation charges in this series of 20CCFBO$_{x\mathrm{Nb/Ta}}$, which provides another perspective to understand the fluorite-pyrochlore-weberite phase stability. In a perfect fluorite structure (without oxygen vacancies), the cation charge should be +4. In the fluorite F1 and F2, the mean cation charges are +3.75 and +3.69, respectively, given 1/16 (in the endmember F1) or more fractions of oxygen vacancies. In a perfect pyrochlore $A_2^{3+}B_2^{4+}O_7$ structure, the mean cation charge should be +3.5, with 3+ cations on the A site and 4+ cations on the B sites. In our 20CCFBO$_{x\mathrm{Nb/Ta}}$ series, from P3 to P8, the mean cation charge decreases from +3.68 to +3.63, as the mean cation charge on the A-site drops from +3.23 to the ideal value of +3, while the mean cation charge on the B-site increases from +4.13 to +4.25. Then, from P8 to P$_W$13, the mean cation charge further decreases from +3.63 to +3.53, as the mean cation charge on the A-site maintains at the ideal value of +3, while the mean cation charge on the B-site decreases from +4.25 to +4.07 (towards the ideal value of +4). In a perfect weberite $C_3^{3+}D^{5+}O_7$ structure, the mean cation charge should also be +3.5, with 3+ cations on the C sites and 5+ cations on the B sites. In our 20CCFBO$_{x\mathrm{Nb/Ta}}$ series, from W13 to W17, the mean cation charge decreases from +3.53 to the ideal value of +3.5, as the mean cation charge on the C sites drops from +3.08 to the ideal value of +3, while the mean cation charge on the D sites increases from +4.88 to the ideal value of +5.

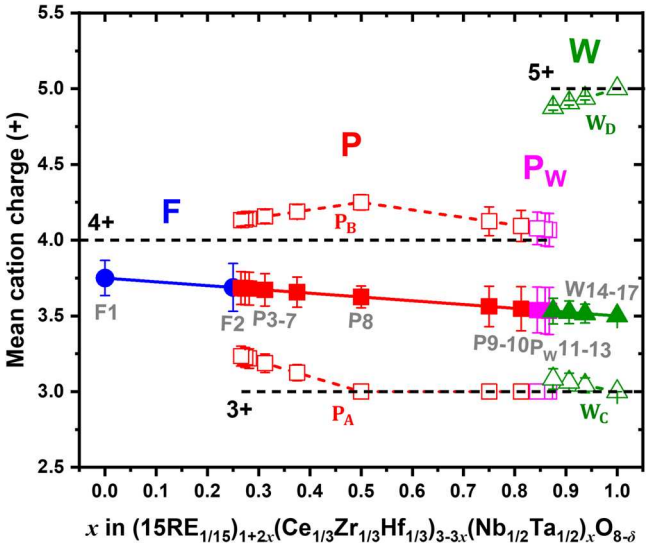

Fig. 8. Mean cation charge *vs.* compositional variable x in this series of 20CCFBO$_{x\mathrm{Nb/Ta}}$ ($0 \le x \le 1$). The solid data points and solid lines represent the overall mean cation charge, while the hollow data points and colored dashed lines represent the mean cation charge on each sublattice for the pyrochlore (P$_A$ and P$_B$) and weberite (W$_C$ and W$_D$) phases. Black dashed lines mark the ideal 3+, 4+, and 5+ charges as references.

Complementing Fig. 8, Fig. 9 displays the fractions of anti-site cations in the pyrochlore and weberite phases. Here, we define anti-site cations as cations with different valence states from ideal values on the sublattices. In the pyrochlore phase, we assume RE^{3+} cations prefer A sites while other +4 (including Ce^{4+}) prefer B sites. Therefore, any +4 cations at the A sites or any +3 and +5 cations at the B sites are anti-site cations. (Note that in this definition Nb^{5+} and Ta^{5+} are anti-site cations on either A or B sites, while they can alternatively be considered as anti-site cations on A sites only in a different definition as they prefer B sites over A sites.) As shown in Fig. 10(a), the fraction of anti-site cations in the A sites reduces in its absolute value from ~0.23 in P3 to 0 in P8, and the fraction of anti-site cations in the B sites increases in its absolute value from ~0.13 in P3 to ~0.8 in P$_W$13. The pyrochlore phase is

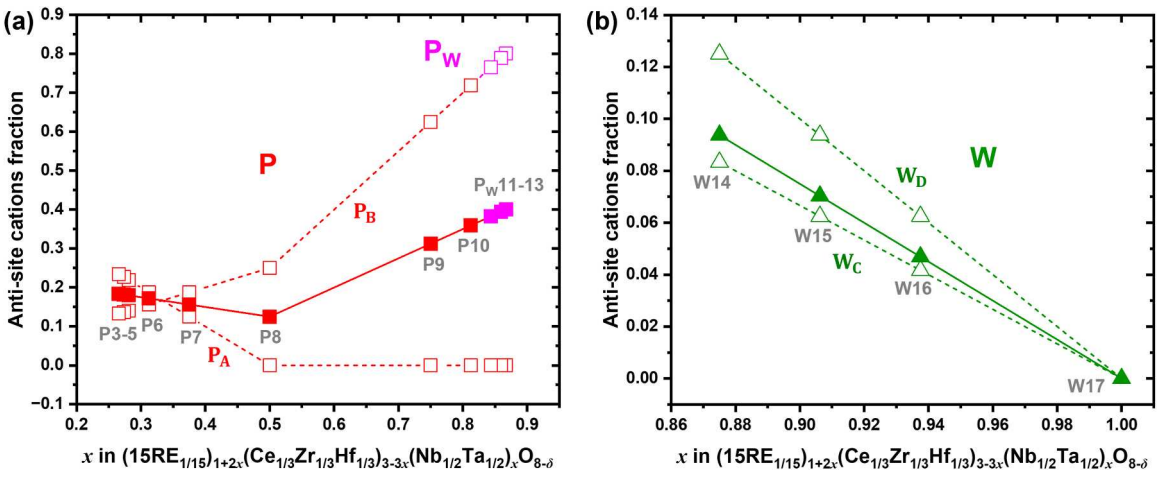

Fig. 9. Fraction of anti-site cations *vs.* compositional variable x in this series of 20CCFBO$_{x\mathrm{Nb/Ta}}$ ($0 \le x \le 1$). The solid data points and solid lines represent the overall fraction of anti-site cations in (a) pyrochlore and (b) weberite, while the hollow data points and dashed lines represent the fraction of anti-site cations on each sublattice of pyrochlore (P_A and P_B) and weberite (W_C and W_D). Here, anti-site cations are generally defined as cations with different valence states from ideal values on the sublattices.

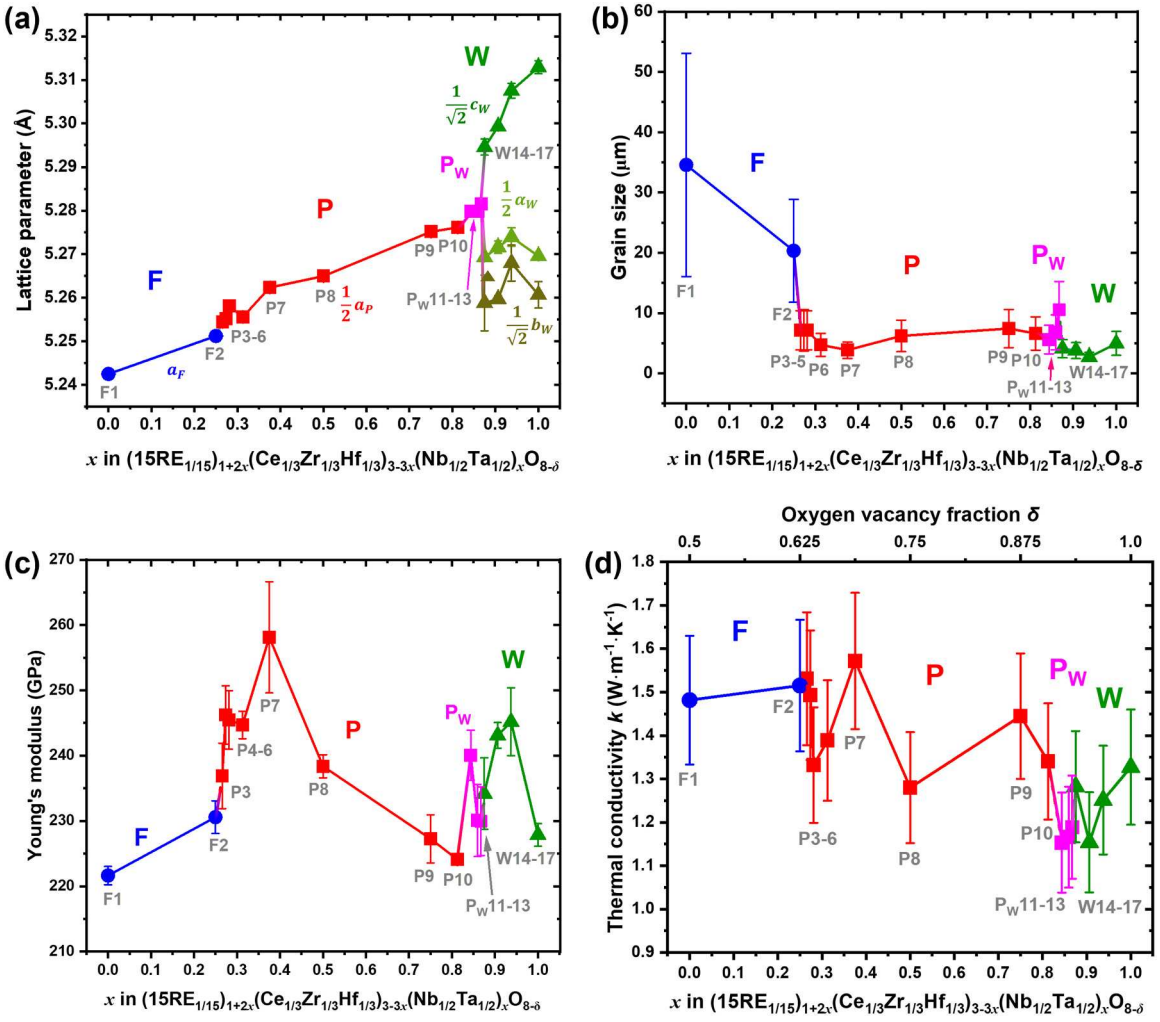

Fig. 10. Measured (a) lattice parameters (α_F for the fluorite, $\alpha_P/2$ for the pyrochlore, and $\alpha_W/2$, $b_W/\sqrt{2}$, and $c_W/\sqrt{2}$ for the weberite), (b) grain size, (c) room-temperature Young's modulus (E), and (d) 200 °C thermal conductivity (k) for the 17 specimens in the 20CCFBOs series with the chemical formula $F1_{1-x}W17_x = [(15RE_{1/15})_1(Ce_{1/3}Hf_{1/3}Zr_{1/3})_3O_{7.5}]_{1-x}[(15RE_{1/15})_3(Nb_{1/2}Ta_{1/2})_1O_7]_x = (15RE_{1/15})_{2x+1}(Ce_{1/3}Zr_{1/3}Hf_{1/3})_{3-3x}(Nb_{1/2}Ta_{1/2})_xO_{8-\delta}$ ($0 \le x \le 1$). The lattice parameters are obtained from unit cell refinements from XRD patterns and are normalized to the primitive fluorite cell (a_F) for comparison.

destabilized (to form the fluorite phase towards the left and form the weberite phase towards the right in Fig. 9(a)) outside this region. As shown in Fig. 3(b), P8 with the lowest fraction of anti-site cations shows a sharp pyrochlore superstructure $(331)_P$ peak (small FWHM), thereby indicating possibly the strong pyrochlore ordering. Yet, P9 has the highest normalized pyrochlore superstructure $(331)_P$ peak intensity and P10 has the smallest FWHM despite higher fractions of anti-site cations on B sites, where some 3+ and 5+ anti-site cations on B sites may compensate each other so that the average charge on B sites reduces and approaches to the ideal 4+ as shown in Fig. 8. Peaks are broadened with decreasing x from P8 to P3 or increasing x from P10 to P_W13, with increasing fractions of anti-site cations. For the weberite phase, W17 has no anti-site cations, and the anti-site cations fractions increase with decreasing x to reach ~0.08 on C-sites and ~0.13 on D sites; beyond these thresholds, the weberite phase de-stabilizes and transits to pyrochlore phase.

In comparison with five-component equimolar high-entropy ceramics, these 20-component CCFBOs have higher configurational entropies (2–2.5 k_B per cation *vs.* ~1.6 k_B per cation), which can in principle provide more entropy stabilization at high temperatures. One interesting observation of this study is that these series of 20CCFBOs possess virtually single ultrahigh-entropy phases with abrupt fluorite-pyrochlore and pyrochlore-weberite transitions. It is yet unclear whether ultrahigh entropies are the main reason for the single-phase stabilization in these 20CCFBOs. We note that these CCFBOs are not equimolar and were not designed to maximize the configurational entropies. In addition, there is long- and short-range ordering in these 20CCFBOs, which also reduces the configurational entropies. The senior author has previously proposed [1,31] that both non-equimolar compositions and short- and long-range ordering in CCCs, while they reduce the configurational entropies, can offer additional dimensions and opportunities to tailor and improve materials properties.

3.5. Properties

Fig. 10 shows the measured lattice parameters, grain sizes, Young's modulus, and thermal conductivities for this series of 17 $20CCFBO_{xNb/Ta}$ specimens.

In Fig. 10(a), the lattice parameters are normalized to that of the primitive fluorite cell (α_F); *i.e.*, we show $\alpha_P/2$ for the pyrochlore phase and $\alpha_W/2$, $b_W/\sqrt{2}$, and $c_W/\sqrt{2}$ for the weberite phase. The gradual increase in normalized lattice parameters with x is mainly due to the increase in the fractions of larger rare earth cations. A (barely noticeable) small jump in the lattice parameter (from α_F to $\alpha_P/2$) is evident at the fluorite-pyrochlore ODT. A large increase (or decrease) from the $\alpha_P/2$ of the pyrochlore lattice P_W13 to $\alpha_W/2$ (or $b_W/\sqrt{2}$ and $c_W/\sqrt{2}$) of the weberite W14 is clearly seen, which resulted from the distortion of the unit cell during the pyrochlore-weberite transition.

Fig. 10(b) shows that the measured mean grain size of the series $20CCFBO_{xNb/Ta}$ decreases with compositional variable x from F1 to W17. This may be attributed to the change of crystal symmetry and structure (phase transsitions) as well as possibly the increase in lattice distortion. In particular, the occurrence of the fluorite-pyrochlore ODT resulted in a substantial reduction in the grain size. The grain growth was significantly slower in both pyrochlore and weberite phases than in the fluorite phase.

Fig. 10(c) shows the measured Young's modulus (E), where no clear trend is identified. Specimen P7 has the highest measured modulus.

In Fig. 10(d), the measured thermal conductivity k demonstrates a general decrease trend with x, but not significantly with large error bars. The minimum measured thermal conductivity (k = 1.1532 ± 0.1153 $W{\cdot}m^{-1}{\cdot}K^{-1}$) was observed in the specimen at P_W11, coinciding with the possible weberite short-range ordering in the long-range pyrochlore phase region. It is known that short-range weberite ordering can result in ultralow thermal conductivity in compositionally complex rare earth niobates from a prior neutron scattering study [39]. Moreover, a drop in k coincides with the presence of weberite-type short-range ordering in the long-range pyrochlore phase was reported in 10-component CCFBOs [29], further supporting this explanation.

Overall, the differences in measured thermal conductivities are small given the relatively large uncertainty in the measurements compared to the overall low thermal conductivities of the samples (1.1–1.6 $W{\cdot}m^{-1}{\cdot}K^{-1}$). However, some interesting trends can be identified (as summarized in Table 2) and discussed as follows. The measured averaged thermal conductivity for the disordered fluorite phase is 1.499 ± 0.002 $W{\cdot}m^{-1}{\cdot}K^{-1}$. The measured averaged thermal conductivity for the ordered weberite phase is appreciably lower (1.254 ± 0.064 $W{\cdot}m^{-1}{\cdot}K^{-1}$). The measured averaged thermal conductivity for the ordered pyrochlore phase without short-range website ordering, 1.423 ± 0.098 $W{\cdot}m^{-1}{\cdot}K^{-1}$, is only slightly lower than that of the disordered fluorite phase (while the difference is within the error bar). Interestingly, the measured averaged thermal conductivity for the pyrochlore phase with the co-existence of short-range website ordering and long-range pyrochlore ordering, 1.169 ± 0.015 $W{\cdot}m^{-1}{\cdot}K^{-1}$, is lower than those of both long-range pyrochlore-ordered phase without short-range website ordering (1.423 $W{\cdot}m^{-1}{\cdot}K^{-1}$) and long-range weberite-ordered phase (1.254 $W{\cdot}m^{-1}{\cdot}K^{-1}$).

4. Conclusions

We designed, fabricated, and investigated a new series of 20-component ultrahigh-entropy $20CCFBO_{xNb/Ta}$ materials, which show an abrupt fluorite-pyrochlore phase transition and an abrupt pyrochlore-weberite phase transition in sequence. Almost all 17 specimens synthesized are in single-phase based in XRD, except that <1 vol% of secondary phases observed in two specimens right before the fluorite-pyrochlore and pyrochlore-weberite phase transitions. The phase evolutions and transitions are carefully characterized by analyzing the characteristic superstructure XRD peak for pyrochlore-fluorite order-disorder transition and peak splitting for pyrochlore-weberite transition with reduced symmetry. Both fluorite-pyrochlore and pyrochlore-weberite phase transitions occur more abruptly than the linear projections of order parameters. Several descriptors are defined and evaluated to analyze phase stability and evolution. The lowest thermal conductivity was observed in the pyrochlore phase with the coexistence of short-range weberite ordering and long-range pyrochlore ordering.

CRediT authorship contribution statement

Jian Luo: Conceptualization, Formal analysis, Funding acquisition, Investigation, Methodology, Project administration, Resources, Supervision, Validation, Visualization, Writing – original draft, Writing – review & editing. **Renkun Chen:** Formal analysis, Writing – review & editing. **Ka Man Chung:** Data curation, Writing – original draft. **Dawei Zhang:** Data curation. **Keqi Song:** Data curation, Formal analysis, Investigation, Visualization, Writing – original draft, Writing – review & editing.

Table 2
Averaged thermal conductivity for each phase in the series of $20CCFBO_{xNb/Ta}$ ($0 \le x \le 1$), where each ± value represents one standard deviation.

	Averaged Thermal Conductivity ($W{\cdot}m^{-1}{\cdot}K^{-1}$)
Fluorite (F1-F2)	1.499 ± 0.002
Pyrochlore without Short-Range Weberite Ordering (P3-P10)	1.423 ± 0.098
Pyrochlore with Short-Range Weberite Ordering (P_W11- P_W13)	1.169 ± 0.015
Weberite (W14-W17)	1.254 ± 0.064

Declaration of Competing Interest

The authors declare that they have no known competing financial interests or personal relationships that could have appeared to influence the work reported in this paper.

Acknowledgments

The work is supported by the National Science Foundation (NSF) in the Ceramics program via Grant No. DMR-2026193.

Appendix A. Supporting information

Supplementary data associated with this article can be found in the online version at doi:10.1016/j.jeurceramsoc.2024.05.058.

References

[1] A.J. Wright, Q. Wang, C. Huang, A. Nieto, R. Chen, J. Luo, From high-entropy ceramics to compositionally-complex ceramics: a case study of fluorite oxides, J. Eur. Ceram. Soc. 40 (2020) 2120–2129, https://doi.org/10.1016/j.jeurceramsoc.2020.01.015.

[2] H. Chen, B. Zhao, Z. Zhao, H. Xiang, F.Z. Dai, J. Liu, Y. Zhou, Achieving strong microwave absorption capability and wide absorption bandwidth through a combination of high entropy rare earth silicide carbides/rare earth oxides, J. Mater. Sci. Technol. 47 (2020) 216–222, https://doi.org/10.1016/j.jmst.2020.02.015.

[3] S. Jiang, T. Hu, J. Gild, N. Zhou, J. Nie, M. Qin, T. Harrington, K. Vecchio, J. Luo, A new class of high-entropy perovskite oxides, Scr. Mater. 142 (2018) 116–120, https://doi.org/10.1016/j.scriptamat.2017.08.040.

[4] J. Gild, M. Samiee, J.L. Braun, T. Harrington, H. Vega, P.E. Hopkins, K. Vecchio, J. Luo, High-entropy fluorite oxides, J. Eur. Ceram. Soc. 38 (2018) 3578–3584, https://doi.org/10.1016/j.jeurceramsoc.2018.04.010.

[5] A.J. Wright, Q. Wang, C. Hu, Y.T. Yeh, R. Chen, J. Luo, Single-phase duodenary high-entropy fluorite/pyrochlore oxides with an order-disorder transition, Acta Mater. 211 (2021), https://doi.org/10.1016/j.actamat.2021.116858.

[6] F. Li, L. Zhou, J.-X. Liu, Y. Liang, G.-J. Zhang, High-entropy pyrochlores with low thermal conductivity for thermal barrier coating materials, J. Adv. Ceram. (2019) 1–7, https://doi.org/10.1007/s40145-019-0342-4.

[7] Z. Teng, L. Zhu, Y. Tan, S. Zeng, Y. Xia, Y. Wang, H. Zhang, Synthesis and structures of high-entropy pyrochlore oxides, J. Eur. Ceram. Soc. (2019), https://doi.org/10.1016/j.eplepsyres.2019.106192.

[8] A.J. Wright, Q. Wang, S.-T.T. Ko, K.M. Chung, R. Chen, J. Luo, Size disorder as a descriptor for predicting reduced thermal conductivity in medium- and high-entropy pyrochlore oxides, Scr. Mater. 181 (2020) 76–81, https://doi.org/10.1016/j.scriptamat.2020.02.011.

[9] M. Qin, H. Vega, D. Zhang, S. Adapa, A.J. Wright, R. Chen, J. Luo, 21-Component compositionally complex ceramics: discovery of ultrahigh-entropy weberite and fergusonite phases and a pyrochlore-weberite transition, J. Adv. Ceram. 11 (2022) 641–655, https://doi.org/10.1007/s40145-022-0575-5.

[10] H. Vega, M. Qin, J. Luo, Thermodynamics of dual-phase compositionally complex ceramics: A case study of ultrahigh-entropy fluorite-bixbyite refractory oxides, J. Eur. Ceram. Soc. 43 (2023) 2104–2114, https://doi.org/10.1016/j.jeurceramsoc.2022.12.033.

[11] Y. Sun, H. Xiang, F.-Z. Dai, X. Wang, Y. Xing, X. Zhao, Y. Zhou, Preparation and properties of CMAS resistant bixbyite structured high-entropy oxides RE_2O_3 (RE= Sm, Eu, Er, Lu, Y, and Yb): Promising environmental barrier coating materials for Al_2O_3f/Al_2O_3 composites, J. Adv. Ceram. 10 (2021) 596–613.

[12] J. Dąbrowa, M. Stygar, A. Mikuła, A. Knapik, K. Mroczka, W. Tejchman, M. Danielewski, M. Martin, Synthesis and microstructure of the (Co,Cr,Fe,Mn,Ni)$_3O_4$ high entropy oxide characterized by spinel structure, Mater. Lett. 216 (2018) 32–36, https://doi.org/10.1016/j.matlet.2017.12.148.

[13] J. Gild, Y. Zhang, T. Harrington, S. Jiang, T. Hu, M.C. Quinn, W.M. Mellor, N. Zhou, K. Vecchio, J. Luo, High-entropy metal diborides: a new class of high-entropy materials and a new type of ultrahigh temperature ceramics, Sci. Rep. 6 (2016) 2–11, https://doi.org/10.1038/srep37946.

[14] M. Qin, Q. Yan, Y. Liu, J. Luo, A new class of high-entropy M_3B_4 borides, J. Adv. Ceram. 10 (2021) 166–172, https://doi.org/10.1007/s40145-020-0438-x.

[15] M. Qin, Q. Yan, Y. Liu, H. Wang, C. Wang, T. Lei, K.S. Vecchio, H.L. Xin, T. J. Rupert, J. Luo, Bulk high-entropy hexaborides, J. Eur. Ceram. Soc. 41 (2021) 5775–5781, https://doi.org/10.1016/j.jeurceramsoc.2021.05.027.

[16] M. Qin, Q. Yan, H. Wang, C. Hu, K.S. Vecchio, J. Luo, High-entropy monoborides: Towards superhard materials, Scr. Mater. 189 (2020) 101–105, https://doi.org/10.1016/j.scriptamat.2020.08.018.

[17] M. Qin, Q. Yan, H. Wang, K.S. Vecchio, J. Luo, High-entropy rare earth tetraborides, J. Eur. Ceram. Soc. 41 (2021) 2968–2973, https://doi.org/10.1016/j.jeurceramsoc.2020.12.019.

[18] J. Gild, J. Braun, K. Kaufmann, E. Marin, T. Harrington, P. Hopkins, K. Vecchio, J. Luo, A high-entropy silicide: $(Mo_{0.2}Nb_{0.2}Ta_{0.2}Ti_{0.2}W_{0.2})Si_2$, J. Mater. 5 (2019) 337–343, https://doi.org/10.1016/j.jmat.2019.03.002.

[19] S. Shivakumar, M. Qin, D. Zhang, C. Hu, Q. Yan, J. Luo, A new type of compositionally complex M_5Si_3 silicides: cation ordering and unexpected phase stability, Scr. Mater. 212 (2022), https://doi.org/10.1016/j.scriptamat.2022.114557.

[20] P. Sarker, T. Harrington, C. Toher, C. Oses, M. Samiee, J.P. Maria, D.W. Brenner, K. S. Vecchio, S. Curtarolo, High-entropy high-hardness metal carbides discovered by entropy descriptors, Nat. Commun. 9 (2018), https://doi.org/10.1038/s41467-018-07160-7.

[21] T.J. Harrington, J. Gild, P. Sarker, C. Toher, C.M. Rost, O.F. Dippo, C. McElfresh, K. Kaufmann, E. Marin, L. Borowski, P.E. Hopkins, J. Luo, S. Curtarolo, D. W. Brenner, K.S. Vecchio, Phase stability and mechanical properties of novel high entropy transition metal carbides, Acta Mater. 166 (2019) 271–280, https://doi.org/10.1016/j.actamat.2018.12.054.

[22] D. Moskovskikh, S. Vorotilo, V. Buinevich, A. Sedegov, K. Kuskov, A. Khort, C. Shuck, M. Zhukovskyi, A. Mukasyan, Extremely hard and tough high entropy nitride ceramics, Sci. Rep. 10 (2020), https://doi.org/10.1038/s41598-020-76945-y.

[23] O.F. Dippo, N. Mesgarzadeh, T.J. Harrington, G.D. Schrader, K.S. Vecchio, Bulk high-entropy nitrides and carbonitrides, Sci. Rep. 10 (2020), https://doi.org/10.1038/s41598-020-78175-8.

[24] Y. Wang, T. Csanádi, H. Zhang, J. Dusza, M.J. Reece, Synthesis, microstructure, and mechanical properties of novel high entropy carbonitrides, Acta Mater. 231 (2022), https://doi.org/10.1016/j.actamat.2022.117887.

[25] P.A. Sukkurji, Y. Cui, S. Lee, K. Wang, R. Azmi, A. Sarkar, S. Indris, S. S. Bhattacharya, R. Kruk, H. Hahn, Q. Wang, M. Botros, B. Breitung, Mechanochemical synthesis of novel rutile-type high entropy fluorides for electrocatalysis, J. Mater. Chem. A Mater. 9 (2021) 8998–9009, https://doi.org/10.1039/d0ta10209a.

[26] T. Wang, H. Chen, Z. Yang, J. Liang, S. Dai, High-entropy perovskite fluorides: a new platform for oxygen evolution catalysis, J. Am. Chem. Soc. 142 (2020) 4550–4554, https://doi.org/10.1021/jacs.9b12377.

[27] X. Chen, Y. Wu, High-entropy transparent fluoride laser ceramics, J. Am. Ceram. Soc. 103 (2020) 750–756, https://doi.org/10.1111/jace.16842.

[28] L. Lin, K. Wang, A. Sarkar, C. Njel, G. Karkera, Q. Wang, R. Azmi, M. Fichtner, H. Hahn, S. Schweidler, B. Breitung, High-entropy sulfides as electrode materials for Li-ion batteries, Adv. Energy Mater. 12 (2022), https://doi.org/10.1002/aenm.202103090.

[29] M. Cui, C. Yang, B. Li, Q. Dong, M. Wu, S. Hwang, H. Xie, X. Wang, G. Wang, L. Hu, High-entropy metal sulfide nanoparticles promise high-performance oxygen evolution reaction, Adv. Energy Mater. 11 (2021), https://doi.org/10.1002/aenm.202002887.

[30] N. Zhou, S. Jiang, T. Huang, M. Qin, T. Hu, J. Luo, Single-phase high-entropy intermetallic compounds (HEICs): bridging high-entropy alloys and ceramics, Sci. Bull. (Beijing) 64 (2019) 856–864, https://doi.org/10.1016/j.scib.2019.05.007.

[31] A.J. Wright, Q. Wang, C. Huang, A. Nieto, R. Chen, J. Luo, From high-entropy ceramics to compositionally-complex ceramics: a case study of fluorite oxides, J. Eur. Ceram. Soc. 40 (2020) 2120–2129, https://doi.org/10.1016/j.jeurceramsoc.2020.01.015.

[32] X.Q. Cao, R. Vassen, D. Stoever, Ceramic materials for thermal barrier coatings, J. Eur. Ceram. Soc. 24 (2004) 1–10, https://doi.org/10.1016/S0955-2219(03)00129-8.

[33] Q. Xu, W. Pan, J. Wang, C. Wan, L. Qi, H. Miao, K. Mori, T. Torigoe, Rare-earth zirconate ceramics with fluorite structure for thermal barrier coatings, : J. Am. Ceram. Soc. (2006) 340–342, https://doi.org/10.1111/j.1551-2916.2005.00667.x.

[34] J. Yang, W. Pan, Y. Han, M. Zhao, M. Huang, C. Wan, Mechanical properties, oxygen barrier property, and chemical stability of RE_3NbO_7 for thermal barrier coating, J. Am. Ceram. Soc. 103 (2020) 2302–2308, https://doi.org/10.1111/jace.16952.

[35] D. Zhang, Y. Chen, T. Feng, D. Yu, K. An, R. Chen, J. Luo, Discovery of a reversible redox-induced order-disorder transition in a 10-component compositionally complex ceramic, Scr. Mater. 215 (2022), https://doi.org/10.1016/j.scriptamat.2022.114699.

[36] D. Zhang, Y. Chen, H. Vega, T. Feng, D. Yu, M. Everett, J. Neuefeind, K. An, R. Chen, J. Luo, Long- and short-range orders in 10-component compositionally complex ceramics, Adv. Powder Mater. 2 (2023), https://doi.org/10.1016/j.apmate.2022.100098.

[37] L. Spiridigliozzi, C. Ferone, R. Cioffi, G. Dell'Agli, A simple and effective predictor to design novel fluorite-structured high entropy oxides (HEOs), Acta Mater. 202 (2021) 181–189, https://doi.org/10.1016/j.actamat.2020.10.061.

[38] L. Xu, H. Wang, L. Su, D. Lu, K. Peng, H. Gao, A new class of high-entropy fluorite oxides with tunable expansion coefficients, low thermal conductivity and exceptional sintering resistance, J. Eur. Ceram. Soc. 41 (2021) 6670–6676, https://doi.org/10.1016/j.jeurceramsoc.2021.05.043.

[39] H. Junjie, H. Guo, L. Jing, T. Jingchao, New class of high-entropy defect fluorite oxides $RE_2(Ce_{0.2}Zr_{0.2}Hf_{0.2}Sn_{0.2}Ti_{0.2})_2O_7$ (RE = Y, Ho, Er, or Yb) as promising thermal barrier coatings, J. Eur. Ceram. Soc. 41 (2021) 6080–6086, https://doi.org/10.1016/j.jeurceramsoc.2021.05.044.

[40] Z. Teng, Y. Tan, S. Zeng, Y. Meng, C. Chen, X. Han, H. Zhang, Preparation and phase evolution of high-entropy oxides $A_2B_2O_7$ with multiple elements at A and B sites, J. Eur. Ceram. Soc. 41 (2021) 3614–3620, https://doi.org/10.1016/j.jeurceramsoc.2021.01.013.

[41] D. Liu, B. Shi, L. Geng, Y. Wang, B. Xu, Y. Chen, High-entropy rare-earth zirconate ceramics with low thermal conductivity for advanced thermal-barrier coatings, J. Adv. Ceram. 11 (2022) 961–973, https://doi.org/10.1007/s40145-022-0589-z.

[42] J. Zhu, X. Meng, J. Xu, P. Zhang, Z. Lou, M.J. Reece, F. Gao, Ultra-low thermal conductivity and enhanced mechanical properties of high-entropy rare earth

niobates (RE_3NbO_7, RE = Dy, Y, Ho, Er, Yb), J. Eur. Ceram. Soc. 41 (2021) 1052–1057, https://doi.org/10.1016/j.jeurceramsoc.2020.08.070.
[43] Z. Zhao, H. Chen, H. Xiang, F.Z. Dai, X. Wang, W. Xu, K. Sun, Z. Peng, Y. Zhou, High entropy defective fluorite structured rare-earth niobates and tantalates for thermal barrier applications, J. Adv. Ceram. 9 (2020) 303–311, https://doi.org/10.1007/s40145-020-0368-7.
[44] Z. Teng, L. Zhu, Y. Tan, S. Zeng, Y. Xia, Y. Wang, H. Zhang, Synthesis and structures of high-entropy pyrochlore oxides, J. Eur. Ceram. Soc. 40 (2020) 1639–1643, https://doi.org/10.1016/j.jeurceramsoc.2019.12.008.
[45] A.J. Wright, Q. Wang, Y.T. Yeh, D. Zhang, M. Everett, J. Neuefeind, R. Chen, J. Luo, Short-range order and origin of the low thermal conductivity in compositionally complex rare-earth niobates and tantalates, Acta Mater. 235 (2022), https://doi.org/10.1016/j.actamat.2022.118056.
[46] A.J. Wright, J. Luo, A step forward from high-entropy ceramics to compositionally complex ceramics: a new perspective, J. Mater. Sci. 55 (2020) 9812–9827, https://doi.org/10.1007/s10853-020-04583-w.
[47] M. Qin, H. Vega, D. Zhang, S. Adapa, A.J. Wright, R. Chen, J. Luo, 21-Component compositionally complex ceramics: discovery of ultrahigh-entropy weberite and fergusonite phases and a pyrochlore-weberite transition, J. Adv. Ceram. 11 (2022) 641–655, https://doi.org/10.1007/s40145-022-0575-5.
[48] A.J. Wright, Q. Wang, C. Hu, Y.-T. Yeh, R. Chen, J. Luo, Single-phase duodenary high-entropy fluorite/pyrochlore oxides with an order-disorder transition, Acta Mater. 211 (2021) 116858, https://doi.org/10.1016/j.actamat.2021.116858.
[49] A.J. Wright, C. Huang, M.J. Walock, A. Ghoshal, M. Murugan, J. Luo, Sand corrosion, thermal expansion, and ablation of medium- and high-entropy compositionally complex fluorite oxides, J. Am. Ceram. Soc. 104 (2021) 448–462, https://doi.org/10.1111/jace.17448.
[50] W. Fan, Y. Bai, Y. Liu, T. Li, B. Li, L. Zhang, C. Gao, S. Shan, H. Han, Principal element design of pyrochlore-fluorite dual-phase medium- and high-entropy ceramics, J. Mater. Sci. Technol. 107 (2022) 149–154, https://doi.org/10.1016/j.jmst.2021.08.018.
[51] E.A. Dean, J.A. Lopez, Empirical dependence of elastic moduli on porosity for ceramic materials, J. Am. Ceram. Soc. 66 (1983) 366–370, https://doi.org/10.1111/j.1151-2916.1983.tb10051.x.
[52] J. Zeng, K.M. Chung, Q. Wang, X. Wang, Y. Pei, P. Li, R. Chen, Measurement of high-temperature thermophysical properties of bulk and coatings using modulated photothermal radiometry, Int. J. Heat. Mass Transf. 170 (2021), https://doi.org/10.1016/j.ijheatmasstransfer.2021.120989.
[53] K.M. Chung, T. Feng, J. Zeng, S.R. Adapa, X. Zhang, A.Z. Zhao, Y. Zhang, P. Li, Y. Zhao, J.E. Garay, R. Chen, Thermal conductivity measurement using modulated photothermal radiometry for nitrate and chloride molten salts, Int. J. Heat. Mass Transf. 217 (2023), https://doi.org/10.1016/j.ijheatmasstransfer.2023.124652.
[54] I. and G.P. Barin, Thermochemical data of pure substances, 1993. https://doi.org/10.1002/9783527619825.
[55] R.D. Shannon, Revised Effective Ionic Radii and Systematic Studies of Interatomie Distances in Halides and Chaleogenides, 1976.
[56] T. Subramani, A. Navrotsky, Energetics of formation and disordering in rare earth weberite RE_3TaO_7 materials, Inorg. Chem. 58 (2019) 16126–16133, https://doi.org/10.1021/acs.inorgchem.9b02675.